Technical University of Denmark

DTU

Compliant electro-thermal microactuators.

Jonsmann, Jacques; Sigmund, Ole; Bouwstra, Siebe

DTU Library
Technical Information Center of Denmark

COMPLIANT ELECTRO-THERMAL MICROACTUATORS

J. Jonsmann, O. Sigmund*, S. Bouwstra
Mikroelektronik Centret, Bldg. 345 east, Technical University of Denmark
*Department of Solid Mechanics, Bldg. 404.
2800 Lyngby, Denmark
e-mail: jacques@mic.dtu.dk

ABSTRACT

This paper describes design, microfabrication and characterisation of topology optimised compliant electro-thermal microactuators. The actuators are fabricated by a fast prototyping process using laser micromachining and electroplating. Actuators are characterised with respect to displacement, force and work, by use of image analysis. Four different actuators are presented. These actuators are capable of displacements of 30 μm and forces of 15 mN. The most recent actuator designs function in reasonable accordance with design predictions.

INTRODUCTION

Microactuators have many prospective areas of application, such as micropositioning, assembly, manipulation etc. Wear in microactuators gives significant problems for actuators utilising multicomponent movable parts. Compliant actuators address this problem by achieving motion by bending of a structural members. Compliant structures are relatively simple to process, are quite robust, inherently stable and systematic design is feasible. Such a systematic design procedure is used for the two dimensional compliant electro-thermal microactuators addressed in this paper. Most microactuators consist of relatively simple geometrical shapes, which makes analytical modeling simple. It is reasonable to assume that such simple geometries will not give optimal actuator designs. As will be shown in this paper, optimised actuators indeed have non-trivial designs.

DESIGN

Two-dimensional compliant electro-thermal microactuators are designed by topology optimisation [1,2,4]. Topology optimisation produces actuator structures which operate within a few percent of the theoretical optimum. Actuation of the actuator structures is based on thermal expansion caused by Joule heating. Thermal actuation has been chosen for its large work density and simple integration with the design algorithms. The actuators are optimised to do maximum work on a specified load spring with stiffness k_l, given the material properties and the following constraints;

- Design domain size
- Location of contacting electrodes
- Location of work point
- Electrical resistance
- Amount of material used
- Available voltage

The optimisation algorithms produce a two-dimensional material distribution in a design domain. Figure 1 shows such a design domain. The material distribution is given in the form of a gray tone image which defines the structure.
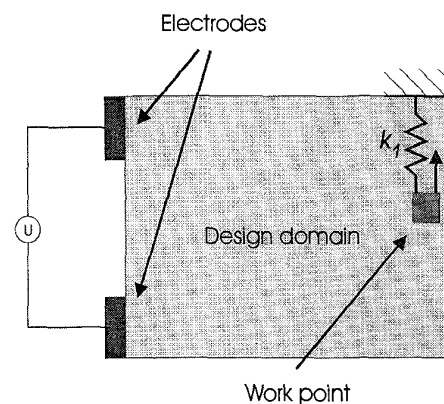

Figure 1. Illustration of a design domain with drive electrodes and work point. At the work point an actuation direction and load spring k_l is indicated.

The images in table 1 show the material distribution for the four actuators presented in this paper. The material distribution defines the current and potential distributions from which the dissipated power distribution follows. Locally calculating the power loss due to heat conduction in the structure and convection into the surrounding air, gives the temperature distribution and thus strain- and displacement distributions. All but the power loss distribution can be calculated with high accuracy. The actuator topologies are optimised by sequential steps of finite element analysis and material redistribution [1,2].

Convection from the structure is very complicated to estimate and simulate. To simplify the convection model we assume that there is a local power loss which is proportional to temperature. The simplification of the convection model is the primary cause for discrepancies between predicted behaviour and results from microfabricated actuators.

Table 1. The upper part of the table lists optimisation input, resulting material distribution and predicted behaviour. The lower part of the table lists measured behaviour of the actuators.

Design parameters				
Actuator number	1	2	3	4
Optimised for load k_l	550 N/m	550 N/m	1370 N/m	1370 N/m
Dimensions Width × Length × Thickness	500 μm × 200 μm × 11 μm	500 μm × 150 μm × 11 μm	500 μm × 200 μm × 16.4 μm	500 μm × 200 μm × 16.4 μm
Material distribution Black indicates material and white indicates void.				
Description	Electrodes at upper and lower left side of the design domain. Work point at the extreme right of the design domain.	Electrodes at upper and lower left side. Work point at the extreme right of the design domain.	Electrodes at each side of the design domain. Work point at central top of the design domain.	Electrodes at each side of the design domain. Work point at central top of the design domain.
Predicted behaviour	2.8 nm/mW * 0.0125 Ω	15.6 nm/mW * 0.190 Ω	69.6 nm/mW 0.078 Ω	31.3 nm/mW 0.185 Ω
Measured behaviour				
Unloaded responsivity c_0	18.0 nm/mW	62.4 nm/mW	23.9 nm/mW	54.5 nm/mW
Structural stiffness k_0	N.A.	N.A.	2782 N/m	1887 N/m
Linear range	3 μm	3 μm	3 μm	2 μm
Specific work for the optimised load k_l	N.A.	N.A.	0.161 pJ/mW^2	0.428 pJ/mW^2
Maximum specific work	N.A.	N.A.	0.182 pJ/mW^2	0.673 pJ/mW^2
Temporal behaviour Time constant and associated frequency	5.5 ms 182 Hz	18.3 ms 55 Hz	11.4 ms 88 Hz	13.4 ms 75 Hz
Electrical resistance	0.026 Ω	0.145 Ω	0.058 Ω	0.130 Ω
Absolute maximum Displacement Force Work	30 μm N.A. N.A.	25 μm N.A. N.A.	17 μm 15.0 mN 22.3 nJ	15 μm 7.7 mN 28.3 nJ

* Based on early estimates of material properties and loss coefficients.

The construction material used in the fabrication of these actuators is electroplated nickel with the following properties: Young's modulus 200 GPa, thermal expansion coefficient $15 \cdot 10^{-6}$ K^{-1}, resistivity 15.7×10^{-6} Ω cm. The convection loss coefficient is experimentally found to be 18.7 kW/K m^2.

The design algorithm assumes small displacements and linear behaviour. All changes in the actuator geometry due to actuation is thus ignored. Changes in material properties due to heating are also not included in the model. These effects give rise to non-linearities as will be shown for the fabricated actuators.

The design algorithms produce two-dimensional structures with in-plane deflections. As the third dimension is not included in the design, out of plane motion can occur for the fabricated actuators. To prevent this the structure must be so thick that thermal strain relief by in-plane motion is more likely than by out of plane buckling.

The structures produced by the design algorithms typically consist of rigid sections connected by flexible hinges in which most of the deformation takes place. A purely two-dimensional behaviour is achieved by ensuring that the flexible hinge compliance is much higher for in-plane motion than for out of plane motion. This is accomplished by fabricating the actuators so that the aspect ratio (thickness over width) at the flexible hinges is high.

Actuator displacement is given by:

$$d = cP \qquad (1)$$

where P is the input power and c the proportionality constant which we in the following refer to as the actuators responsivity. Responsivity depends on the load k_l:

$$c = \frac{c_0 k_0}{k_0 + k_1} \qquad (2)$$

where k_0 is the actuators structural stiffness at the work point.

We define power specific work W' as the work done by the actuator on the load k_1, per input power squared. Power specific work depends on the load:

$$W' = \frac{bk_1}{(k_0 + k_1)^2} \qquad (3)$$

The actuator structure resulting from the topology optimisation is the optimum structure for the given design constraints, thus it is the structure which does maximum work on the load k_1. That the actuator is the optimal structure for driving a load of k_1, does not imply that the actuator itself performs optimally for a load of k_1. Any actuator will do maximum work on a load, which is equal to the actuators work point stiffness k_0. We have observed that for the topology optimised structures k_0 is always larger than k_1. This phenomenon is not fully understood, but is believed to be related to non-reversible work transformations in the structure.

FABRICATION

To ensure a purely two-dimensional behaviour of the actuators, it is necessary to fabricate the structures with vertical sidewalls and aspect ratios higher than 1 at the flexible hinges. For aspect ratios less than 1, out of plane buckling could occur more easily.
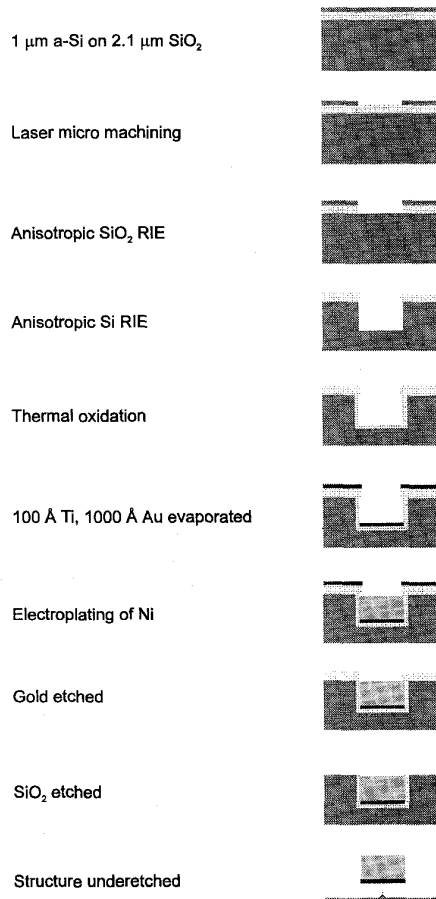
1 μm a-Si on 2.1 μm SiO₂

Laser micro machining

Anisotropic SiO₂ RIE

Anisotropic Si RIE

Thermal oxidation

100 Å Ti, 1000 Å Au evaporated

Electroplating of Ni

Gold etched

SiO₂ etched

Structure underetched

Figure 2. Process sequence.

590

The process sequence by which these actuators are made is shown in figure 2. Metallic actuator structures are made by electroplating nickel in a silicon mold. Mold definition is done by laser micromachining of a silicon RIE mask in a chlorine atmosphere [3,4,5]. Laser micromachining allows smaller feature sizes and faster prototyping of new structures, as compared to traditional photolithography. The laser micromachined silicon pattern is transferred to an underlying siliconoxide by anisotropic RIE. The siliconoxide is used as the final etch mask for deep anisotropic RIE of the silicon mold. Subsequent thermal oxidation of the mold ensures an electrically insulating layer to prevent unwanted precipitation during electroplating. A gold evaporation gives the base layer for electroplating. A brief gold etch ensures that any unwanted gold layer on the sidewalls is removed. Such a sidewall metallisation would otherwise create a short circuit to the gold on the top surface, with unwanted plating as a result. A thick nickel layer is electroplated in the mold, and non-contacted gold and the SiO₂ mask is etched away. The nickel structures are released by dry underetching of silicon in a CF₄/O₂ plasma.

In figures 3-6 SEM images of the four example actuators presented in this paper are shown. An interesting phenomenon is seen in the SEM images, underetching of the nickel structures are proceeding at an accelerated rate in the presence of nickel. This can be seen in the SEM images as the recesses below the structures. This effect is caused by heating of the nickel by interaction with the electro-magnetic field producing the plasma in the barrel etcher in which the underetching is done. The heated nickel in turn heats both the nearby silicon and the plasma, thus the silicon etching proceeds faster. In close proximity of the nickel, the silicon etch rate is 2 μm/min in contrast to 0.25 μm/min at a distance from the nickel. This produces an anisotropic underetch in which the lateral etch rate is 8 times higher than the vertical etch rate.
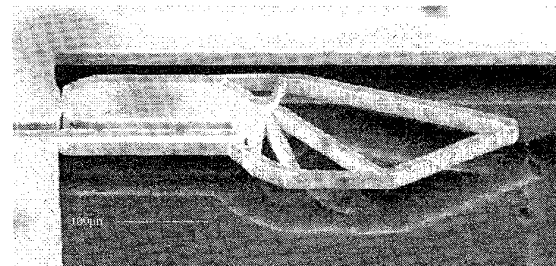

Figure 3. SEM image of actuator 1.
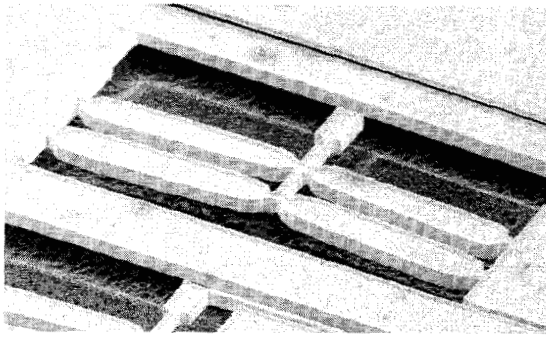

Figure 4. SEM image of actuator 2.
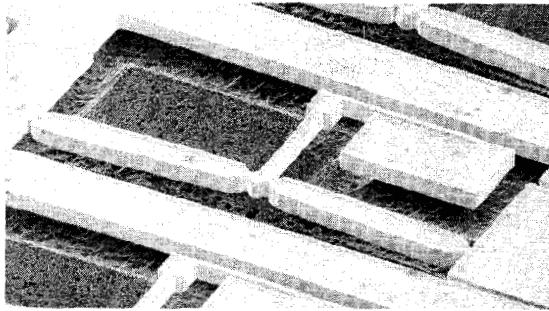
Figure 5. SEM image of actuator 3.

Figure 6. SEM image of actuator 4. Note the blade spring attached at the work point.

CHARACTERISATION

The main parameters of interest for these actuators are displacement, exerted force and work done, when the actuator is working against a given load, ie. spring stiffness. To accomplish this, actuator structures with several different loads attached at the work point are fabricated. An example of such a structure with a blade spring acting as the load, is shown in figure 6. The spring constant of the load k_l is adjusted for each structure by varying the beam length of the blade spring. Knowing the load for a given structure and measuring the work point displacement during actuation, gives both the exerted force and the work done on the load.

Dissipated power is controlled by passing a known current through the structure and measuring the voltage drop across the structure. This is done much like a four point measurement. Two probes are used to pass the current through the structure, and other two probes are used to measure the voltage drop.

The actuator displacement is measured by image analysis of images of the work point, acquired by a framegrabber and a CCD camera attached to a probe microscope. For each input power an image is grabbed and displacement information is found by comparison of neighbouring images in the image sequence. This approach enables us to measure displacements with an accuracy of 20 nm. A schematic drawing of the characterisation set-up is shown in figure 7.
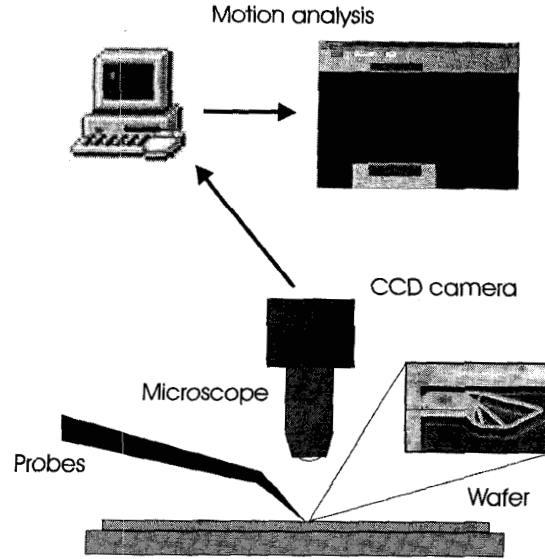

Figure 7. Experimental set-up. Images of the actuator work point, are acquired by a CCD camera and a framegrabber. Work point motion is determined by image analysis.

In the following the characteristics of actuator 4 will be presented. Table 1 lists the predicted and measured characteristics of all four actuators.

Figure 8 shows a typical displacement and force characteristic.
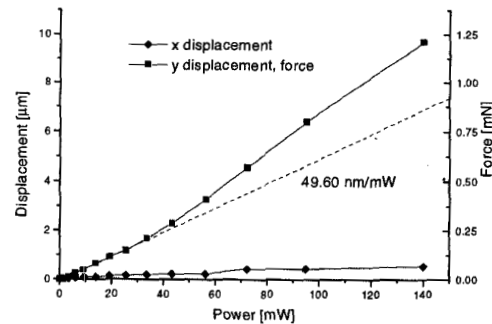

Figure 8. Displacement and force vs. dissipated power, for actuator 4 driving a 124 N/m load.

For the displacement vs. power characteristic we observe the expected linear behaviour at low powers. The slope at low powers is used as the responsivity. At higher powers the actuator displays a significant non-linearity. We observe increased responsivity for intermediate powers and a decreasing responsivity for high powers. Several effects produce this non-linearity. Structural stiffness k_0 and thus responsivity is affected by both geometrical changes resulting from the actuator deflection, and material softning due to the elevated temperatures. At intermediate powers geometrical changes in the structure produce a higher structural stiffness k_0 which increase the responsivity. At high powers material softning will lower k_0 and thus lower

responsivity. Responsivities and power specific work for 6 different loads are plotted in figures 9 and 10, respectively. The actuator performs in accordance with the theory as indicated by the curve fits. From the curve fit in figure 9 a structural stiffness k_0 =1887 N/m is found.

$$Fit: c = \frac{c_0 k_0}{k_0 + k_1}$$
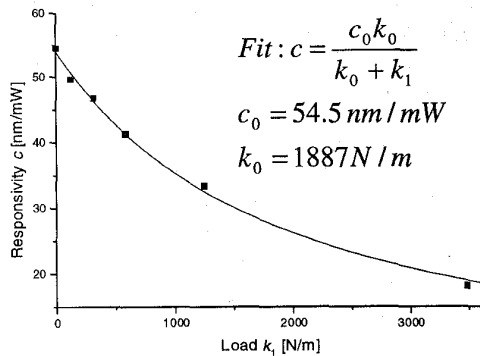
$$c_0 = 54.5\,nm/mW$$

$$k_0 = 1887\,N/m$$

Figure 9. Responsivity vs. applied load for actuator 4.

In the work characteristic in figure 10, a clear maximum is seen for a load around k_0. As discussed in the design section, the structural stiffness k_0=1887 N/m is higher than the load for which the actuator is optimised, k_l=1370 N/m.

$$Fit: W' = \frac{bk_1}{(k_0 + k_1)^2}$$
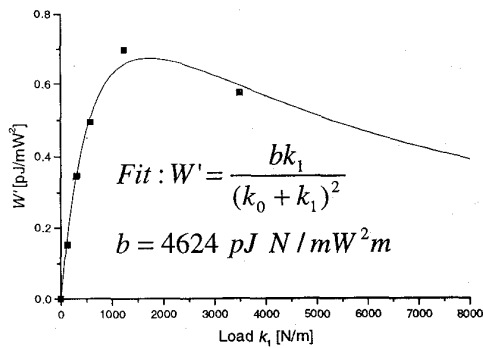
$$b = 4624\ pJ\ N/mW^2 m$$

Figure 10. Power specific work vs. applied load for actuator 4.

Figure 11 shows actuator resistance as a function of displacement. For small displacements the resistance varies linearly with displacement, thus making position feedback feasible.
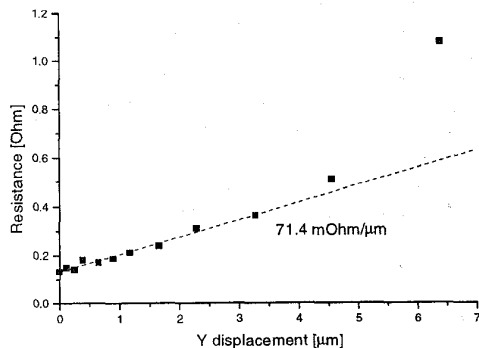

71.4 mOhm/µm

Figure 11. Resistance vs. displacement for an unloaded actuator 4.

Resistance changes are due to geometrical changes in the structure and resistivity changes caused by the elevated temperature. Although the resistance characteristic in figure 11 looks promising, this feedback scheme is complicated by the fact that the change in resistance primarily is due to temperature changes, not geometrical changes. For a given temperature and thus resistance, the displacement is dependent on the load. Position feedback using the electrical resistance is therefore only possible for known loads.

$$Fit: T_1 = \frac{P_0}{\sqrt{C^2 \omega^2 + q^2}}$$
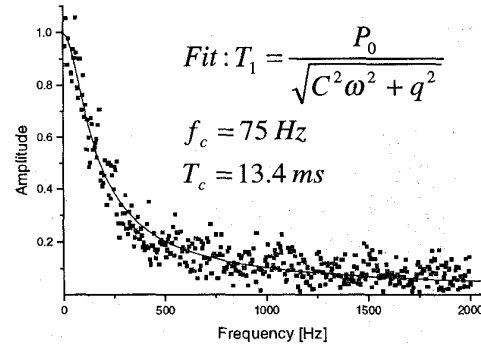
$$f_c = 75\,Hz$$

$$T_c = 13.4\,ms$$

Figure 12. Normalised amplitude vs. frequency for actuator 4.

Figure 12 shows the actuators frequency response. The frequency response is measured using a fiber optic proximity sensor [6].

Displacement amplitude is proportional to temperature amplitude which is given by:

$$T_1 = \frac{P_0}{\sqrt{C^2 \omega^2 + q^2}} \tag{4}$$

where P_0 is the power amplitude, C and q is characteristic heat capacity and heat transport, respectively. ω is the angular frequency. –3 dB bandwidth and associated time constant is found by curve fitting the theoretical behaviour to the measured response function, to be 75 Hz and 13.4 ms, respectively.

Figures 13-15 show measured temperature distributions. Figure 13 shows an infrared image of the actuated structure. It is apparent that the central part of the structure has the highest temperature. Unfortunately the CCD camera by which these images are taken is not sensitive to the long wavelengths associated with room temperature, so only temperatures above approximately 200 °C are shown in the image. Figure 14 shows isothermal curves obtained from the IR image in figure 13. Figure 15 shows a daylight image of the actuator with the isothermal curves superimposed.
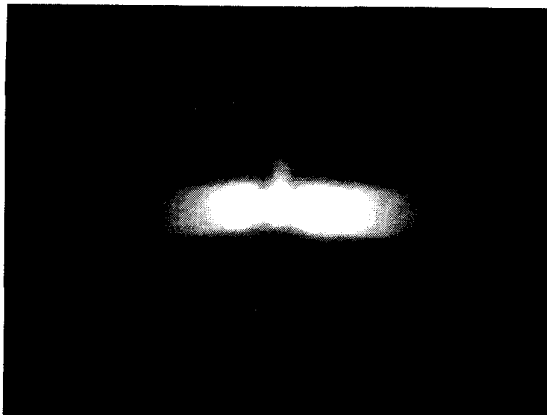
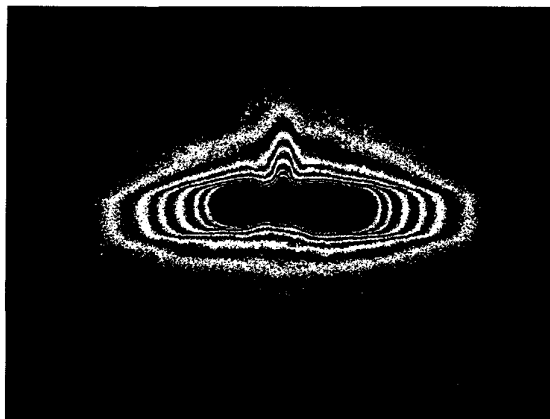Figure 13. Infrared emission image of the actuated structure.

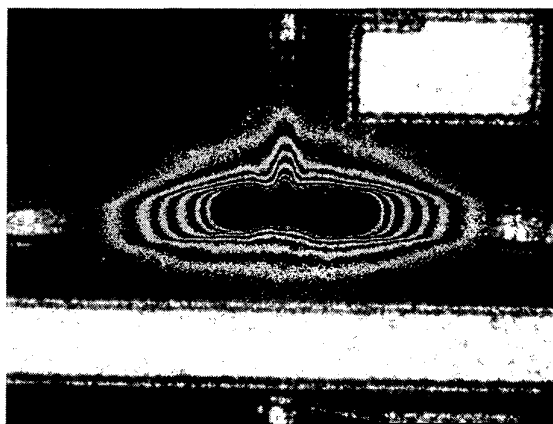Figure 14. Isothermal curves obtained from the emission image in figure 13.

Figure 15. Image of the actuator with superimposed isothermal curves.

DISCUSSION

Theoretical considerations show that actuators designed by this topology optimisation method, operate at or close to an optimum. This however is virtually impossible to prove experimentally. Experimentally we can evaluate the design models by comparing experimental and predicted actuator behaviour. An important aspect of this work is therefore to provide experimental feedback to the design algorithms. The topologies of the designed structures depend on material properties and the convective power loss constant, which can only be determined experimentally. For actuators 1 and 2 the material properties were not well known at design time, and the convective loss constant had been found by grossly extrapolating classical convection models. The significant dicrepancy between predicted and measured behaviour is accredited to this fact. Actuators 3 and 4 are based on measured material properties and the results obtained from actuators 1 and 2. For actuators 3 and 4 the predicted and measured behaviour is much closer, which shows great promise for future actuators designed using this topology optimisation scheme. For the latest actuator designs, fabrication inaccuracies account for most of the discrepancy between predicted and measured behaviour.

CONCLUSION

In this paper design, fabrication and characterisation of topology optimised compliant electrothermal microactuators is described. The actuators are fabricated by a fast prototyping process, using electroplating of nickel in a silicon mold. The silicon mold is made by laser micromachining and reactive ion etching. Actuators are characterised using image analysis giving a very high accuracy on the obtained results. The most recently fabricated actuators behave in reasonable accordance with design predictions. Fabricated actuators are capable of displacements of 30 μm and forces of 15 mN.

ACKNOWLEDGEMENTS

REFERENCES

[1] O. Sigmund, *Systematic design of MEMS using topology optimization*, SPIE Proc., vol. 3328, p. 23-31, 1998.
[2] O. Sigmund, *On the design of compliant mechanisms using topology optimization*, Mech. of Structures and Machines, vol. 25, num. 4, p. 495-526, 1997.
[3] J. Jonsmann, O. Sigmund, S. Bouwstra, *Compliant thermal microactuators*, Proc. Eurosensors XII, 1998.
[4] U. D. Larsen, O. Sigmund, S. Bouwstra, *Design and fabrication of compliant mechanisms and material structures with negative Poisson's ratio*, J. of MEMS, vol. 6, p. 99-106, 1997.
[5] M. Müllenborn, M. Heschel, U. D. Larsen, H. Dirac, S. Bouwstra, *Laser direct etching of silicon on oxide for rapid prototyping*, J. Micromech. Microeng., vol. 6, p. 49-51, 1996.
[6] J. Jonsmann, S. Bouwstra, *Membrane parameter extraction from resonance frequencies*, Proc. Eurosensors X, p. 183-186, 1996.